Robust substrate anchorages of silk lines with extensible nano-fibres

Jonas O. Wolff[1][*][,a], Daniele Liprandi[2][,a], Federico Bosia[3], Anna-Christin Joel[4], and Nicola M. Pugno[2][,5][,]**

[1] Department of Biological Sciences, Macquarie University, Sydney, NSW 2109, Australia

[2] Laboratory of Bio-inspired, Bionic, Nano, Meta Materials & Mechanics, Department of Civil, Environmental and Mechanical Engineering, University of Trento, Via Mesiano 77, I-38123 Trento, Italy

[3] Department of Applied Science and Technology, Politecnico di Torino, Corso Duca degli Abruzzi 24, 10129, Torino, Italy

[4] Institute of Biology II, RWTH Aachen University, Worringerweg 3, 52074 Aachen

[5] School of Engineering and Materials Science, Queen Mary University, Mile End Rd, London E1 4NS, UK

[*] corresponding author: jonas.wolff@mq.edu.au
[**] corresponding author: nicola.pugno@unitn.it
[a] These authors contributed equally to this work.

29   **Abstract**

30   Living systems are built of multiscale-composites: materials formed of components with

31   different properties that are assembled in complex micro- and nano-structures. Such biological

32   multiscale-composites often show outstanding physical properties that are unachieved by

33   artificial materials. A major scientific goal is thus to understand the assembly processes and the

34   relationship between structure and function in order to reproduce them in a new generation of

35   biomimetic high-performance materials. Here, we tested how the assembly of spider silk nano-

36   fibres (i.e. glue coated 0.5μm thick fibres produced by so-called piriform glands) into different

37   micro-structures correlates with mechanical performance by empirically and numerically

38   exploring the mechanical behaviour of line anchors in an orb weaver, a hunting spider and two

39   ancient web builders. We demonstrate that the anchors of orb weavers exhibit outstanding

40   mechanical robustness with minimal material use by the indirect attachment of the silk line to

41   the substrate through a soft domain ('bridge'). This principle can be used to design new artificial

42   high-performance attachment systems.

43

44

45

46   **Keywords**

48

1. Introduction

The materials that living systems are built of and produce often display mechanical properties that outperform most man-made materials. This is largely attributed to the specific nano- and micro-composite structure of such materials: by the combination of components with distinct properties and their specific spatial arrangement, the resulting material exhibits a mix of characteristics that is usually not possible to achieve with independent phases or homogeneous (and isotropic) bulk materials (1). Biological composites are also common among adhesive secretions and organs used by organisms to achieve substrate attachment, such as in spider silk anchors (2), mussel byssus threads (3) and gecko feet (4). This is in contrast to artificial adhesive joints that are usually based on homogeneous bulk materials. A better understanding of the structure-function relationships in biological structured adhesives could inspire a new generation of adhesive systems and fasteners with previously unachieved properties (5, 6).

Spider web anchors are micro-structures that serve as attachments for silk lines. Unlike most other biological composite structures and materials, such as bone, nacre or wood, these micro-structures are rapidly formed by the instant spinning of fibres from a secretion stock and their behavioural assembly into distinct architectures. As the fibre arrangement affects the mechanical properties of the structure, a spider can tailor the end-product for different needs using the same base material (7). These features make spider silk anchors very interesting for the bio-inspiration to design instant attachments with tailored properties. However, a successful implementation into a bio-inspired design is still hindered by a limited understanding of the functional role of the material mix and spatial distribution of mechanical properties in silk anchorages.

Silk anchors attach a structural thread, the dragline, to the substrate by a plaque (membrane) that is composed of numerous adhesive nano-fibres (diameter ~0.5 μm). The base material of the plaque is the so-called *piriform silk*. Tensile stress tests of this special type of silk have revealed that it is three times more extensible than the common dragline silk (*major ampullate silk*) (8, 9).

Previous research has shown that the morphology of spider web anchors can be approximated as a tape-like membrane with the dragline fused along the central axis (10). The location where the dragline exits the membrane ('loading point') thereby affects the maximal force the anchor can sustain under tensile load (10). If the dragline is stressed, the membrane is locally deformed and detaches from the substrate surface, along what is referred to as "peeling line". Membrane delamination thus leads to a changing -often growing- peeling line. After

83   Kendall's peeling theory (11) the peeling force of elastic films emerges as proportional to the

84   length of the peeling line. It can be empirically observed, that if the anchor loading point is

85   close to the membrane edge, the peeling line is roughly V-shaped, whereas it is concentric when

86   the loading point is in a central position developing a larger length before meeting the

87   membrane edge (10). Previous comparative measurements and numerical simulations

88   uncovered that dragline placement modulates the anchor's strength, with the 'centrality' of the

89   dragline joint c_d (i.e. the distance between the loading point and the front edge of the anchor

90   membrane divided by the membrane length) being the main determinant of anchor performance

91   within species (10, 12).

92   It remains uncertain how the differences in mechanical properties of the attachment silk

93   and the dragline affect anchor strength, and if there is an optimal ratio of extensible and stiff

94   materials combined in the anchorage. Also, explorative studies have shown that the structure

95   of the dragline joint differs between species, with the dragline being either directly embedded

96   in the piriform silk film in some or suspended in a flexible network of piriform fibres (called

97   'bridge') in others (13) (Fig. 1). The bridge is built of the same material as the silk film applied

98   to the substrate (the plaque). However, while in the plaque the piriform fibres are arranged in a

99   lattice-like structure, they form a radial network of branching bundles in the bridge (Figs. 1h,

100 p). This may reduce stress concentrations in the loading point and enhance anchor resistance at

101 steep pulling angles. A previous in-depth study on the anchorages of the golden orb weaver

102 *Trichonephila plumipes* revealed that the bridge was asymmetric with a stronger expression in

103 the upstream (i.e. the leaving) dragline insertion (10). When pulling on the upstream dragline,

104 a higher force was required to detach the anchor from a polymer surface than when pulling on

105 the downstream dragline, were the bridge was much smaller (10). Therefore, we hypothesized

106 that the bridge enhances the overall robustness of the anchorage. To test this conjecture, we

107 combined an empirical and a numerical study of anchor detachment mechanics in four species

108 that differ in the structure of the dragline joint.

109

110 **2. Results**

111 *2.1. Effects of structure on silk anchor mechanics*

112   For the comparative analysis of anchor mechanics, four species were chosen that

113 differed in their silk ecology and silk anchor structure. The Southern house spider *Kukulcania*

114 *hibernalis* (Fig. 1a) and the Tasmanian cave spider *Hickmania troglodytes* (Fig. 1b) are ancient

115 sheet web builders that barely changed over a long evolutionary timescale. Both species build

116 sheet webs, but while in *K. hibernalis* the sheet is placed directly on the substrate surface, the

117   sheet of *H. troglodytes* is horizontally suspended between rocks which may mechanically be

118   more demanding. The huntsman *Isopeda villosa* (Fig. 1c) is an arboreal hunting spider that uses

119   dragline to secure itself but does not build webs for prey capture. The golden orb weaver

120   *Trichonephila plumipes* (Fig. 1d) is a large aerial web builder and represents the most advanced

121   silk use.

122   We found that in *K. hibernalis* the dragline was directly incorporated into the membrane,

123   with single strands separately following the looping patterns of the piriform silk fibres (Figs.

124   1e, j, r). In the three other species, the dragline fibres were bundled and did not follow the

125   looping patterns of piriform silk fibres in the membrane but were oriented along the middle axis

126   of the more or less axial-symmetrical membrane. While the dragline bundle was attached on

127   top of the membrane in *H. troglodytes* (Figs. 1f, l, s), it was suspended in a radial network of

128   piriform fibre bundles (called piriform silk *'bridge'*) in *T. plumipes* (Figs. 1h, p, u; see also 3D-

129   reconstruction and sections in Wolff & Herberstein (10)). A piriform silk bridge was also

130   present in *I. villosa*, but to a lesser extend (Figs. 1g, n, t).

131   We compared the nominal anchor strength F_{max}/A of the anchors of the four species as

132   the maximal pull off force divided by the plaque area, by pulling off the samples

133   perpendicularly from a (here polypropylene) surface. Nominal strength differed between all

134   species (*K. hibernalis – H. troglodytes*: $p=0.037$; *K. hibernalis – I. villosa*: $p<0.001$; *K.*

135   *hibernalis – T. plumipes*: $p<0.001$; *H. troglodytes – I. villosa*: $p=0.030$; *H. troglodytes – T.*

136   *plumipes*: $p<0.001$; *I. villosa – T. plumipes*: $p=0.015$). It was higher in anchors with a bridge

137   than in those without a bridge. Anchors of *T. plumipes* yielded a ten times higher strength than

138   the anchors of *K. hibernalis*, on average (Fig. 2a). We further analysed the relationship between

139   c_d and F_{max}. Due to the intraspecific variation of silk anchors, we could obtain and measure

140   samples covering a range of c_d values. In all species, F_{max} was a clear function of c_d (*K.*

141   *hibernalis*: $R^2 = 0.554$, $p = 0.006$; *H. troglodytes*: $R^2 = 0.550$, $p = 0.001$; *I. villosa*: $R^2 = 0.576$,

142    $p < 0.001$; *T. plumipes*: $R^2 = 0.624$, $p < 0.001$). However, assuming a linear relation $F_{max}/A = a \cdot c_d$,

143   slopes varied between species from low in *K. hibernalis* ($a = 6.97$ mN/mm^2) to steep in *T.*

144   *plumipes* ($a = 34.28$ mN/mm^2) (Fig. 2b).

145   In addition to perpendicular ($\theta = 90°$) pull-off tests, we performed similar tests at $\theta = 0°$

146   (i.e. along the dragline, parallel to the substrate) and $\theta = 180°$ (dragline flipped over) in all

147   species except *K. hibernalis*. We found that F_{max} was highest at $\theta = 0°$ in all species. However,

148   the reduction of anchor resistance at $\theta = 90°$ and $\theta = 180°$ differed between species (Figs. 3b,

149   d, f). Notably, F_{max} was negatively proportional to the pull-off angle in *H. troglodytes* (0° vs.

150   90°: $p<0.001$; 0° vs. 180°: $p<0.001$; 90° vs. 180°: $p=0.909$) (Figs. 3a, b), while force drops were

151 highest at $\theta = 90°$ in *I. villosa* (0° vs. 90°: $p<0.001$; 0° vs. 180°: $p=0.001$; 90° vs. 180°: $p=0.001$)

152 (Figs. 3 c, d) and *T. plumipes* (0° vs. 90°: $p<0.001$; 0° vs. 180°: $p<0.900$; 90° vs. 180°: $p<0.001$)

153 (Figs. 3 e, f). Force-distance plots indicated that initial stiffness values of anchor joints were

154 similar in all three loading situations for *H. troglodytes* (Fig. 3a) and *I. villosa* (Fig. 3c).

155 However, in *T. plumipes* increasing pull-off angles led to decreased anchor stiffness and higher

156 deformation of the silk joint (Fig. 3e). Furthermore, the proportion of silk anchors that failed

157 by internal fracture before substrate detachment were lowest in *T. plumipes* (pie charts in Fig.

158 3f), indicating that here interfacial stress concentrations were prevented by structural means

159 and in general that anchors work roughly around the uniform strength for peeling and fracture

160 (optimal) condition. A closer inspection of the force-distance curved revealed that the initial

161 slopes (indicating the structural stiffness) were more or less similar in all loading situations in

162 both *H. troglodytes* and *I. villosa*, but decreased with an increasing loading angle in *T. plumipes*.

163 This indicates that stress level is mitigated by structures with different stiffness in the latter

164 species, with a greater concentration on a stiffer structure at low angles and a greater

165 concentration on a softer structure at steep angles. To rationalize these complex observations,

166 we performed ad hoc *in silico* experiments.

167

168   *2.2. Model properties*

169   Numerical simulations can help to clarify the mechanisms of anchor detachment and

170 investigate the influence of the mechanical and geometrical parameters, as the possibility of

171 experimental manipulation is limited. We developed a numerical approach for the three-

172 dimensional deformation and detachment of an elastic membrane (approximating the silk

173 anchorages) of variable geometry and elastic properties, modelled as a spring lattice adhering

174 to a rigid substrate through a cohesive interface (14). Spider-silk is a non-linear elastic material

175 characterized by a yielding-hardening stress-strain law (8). However, as documented in the

176 Supplementary Material, by implementing a cubic law stress-strain law, there are limited

177 variations of the maximal pull-off forces (on average 10.8% lower than in the linear case) and

178 elongations (on average greater by 19.4%). These changes are smaller than the ones deriving

179 from the variation of other model parameters (e.g. thickness, adhesive energy per unit area).

180 Furthermore, no qualitative changes were observed in the mechanical response of the structures.

181 Therefore, for the sake of simplicity, results are presented here for a linear elastic law. This

182 model correctly reproduces known theoretical results for the delamination of single or multiple

183 tapes (11, 15) or membranes in simple loading cases (16).

184   For this study, three regions were identified in the elastic membrane: a stiffer fibre
185   (corresponding to the embedded dragline), a circular bridge and a rectangular plaque. The
186   dragline was embedded in the bridge with a variable exit point to perform parametric tests on
187   the centrality parameter c_d. This choice was made after analysing the results of parametric tests
188   shown in S1.

189   These parametric studies show that results could be grouped for small (<45°) and large
190   pulling angles (>120°). In our tests, we thus chose 15°, 90° and 165° as indicative angles to
191   describe small, normal, and large angle loading, respectively (See S1, Figs. S2 and S3). We
192   constructed each a set of models for the anchors of *T. plumipes*, *I. villosa* and *H. troglodytes*,
193   with the specific shape and dragline joint location, using the average geometric variables
194   measured for each species (Tab. 1). Silk membrane stiffness was derived from tensile tests of
195   carefully delaminated silk anchors of *T. plumipes*, *I. villosa* and *H. troglodytes* (9, 12) (further
196   details in S1). Anchors of *K. hibernalis* could not be handled in this setup due to their small
197   size and, accordingly, were omitted. Piriform silk membranes generally had a 10-40 times
198   smaller stiffness than dragline silk of these or related species (17-19) (Tabs. 1, S1). Silk
199   membranes of *T. plumipes* were six times stiffer and stronger than the membranes of *I. villosa*
200   and *H. troglodytes*, on average. This may be due to the grid-like overlay of fibres within the
201   membrane (2) caused by the specific back-and-forth spinning pattern in this spider (10).

202   A bridge structure was not found in silk anchors of *H. troglodytes*. The effective stiffness
203   of the bridge in *T. plumipes* and *I. villosa* could not be experimentally determined, but based
204   on our structural analysis we presumed a lower stiffness than the plaque, as piriform fibres are
205   barely cross-linked in the bridge, in contrast to the plaque. Furthermore, the bridge contains
206   unstretched, twisted fibres (10) that may contribute to a high extensibility of this structure. We
207   therefore modelled the bridge of *T. plumipes* as 100 times softer than the plaque. The species-
208   specific bridge geometry was modelled based on the microscopy observation of the silk anchors
209   (Tab. 1). In contrast, for *I. villosa* the bridge was modelled as an initially detached circular area
210   around the dragline with the same stiffness as the plaque.

211   The effect of the positioning of the dragline on the pull-off force is illustrated in detail
212   in the supplementary material, in particular in Figs S1.12.

213   No model was constructed for *K. hibernalis*, due to the unclear mechanical properties
214   of its silk and the complicated arrangement of dragline fibres in its anchors, which is arduous
215   to implement numerically.

216

217   *2.3. Critical role of silk bridge for anchor robustness*

218   At first, we verified our models by replicating the peeling tests *in silico*. Figures 3g, i
219   and k show the simulated load-displacement curves for different loading angles. For the model
220   of *H. troglodytes*' anchors (Fig. 4a), we observed a decrease in anchor strength for increasing
221   loading angles in agreement with the empirical observation (Fig. 3g). However, we did not
222   observe the decrease in maximal extensibility. This can be attributed to simplifications in the
223   numerical model, which does not account for membrane tearing effects during delamination or
224   a possible anisotropy of the membrane structure.

225   For the model of *I. villosa*'s anchors, we implemented a detached area centred in the
226   middle of the dragline and with a slightly greater diameter than the dragline length (Fig. 4b).
227   We observed a larger force value and structural stiffness for small pulling angles, whereas
228   similar forces and extensibility were found for loading angles of $\theta = 90°$ and $\theta = 165°$ (Fig. 4i).
229   This improved extensibility for high pulling angles is given by the elongation allowed by the
230   detached area.

231   For the model of *T. plumipes*' anchors, we implemented a soft bridge centred in a point
232   belonging to the dragline and displaced by 0.08 mm with respect to the centre (Fig. 4c). The
233   diameter of the bridge is 0.5 mm, which is 0.1 mm greater than the dragline length. This causes
234   the rear of the dragline to be connected directly to the plaque only in for a small length, as found
235   in a previous in-depth microscopy study (10). We observed a strong correlation between the
236   structural stiffness and the pulling angle (Fig. 3k). The peak of the force-displacement curves
237   were points of extreme instability of the membrane, corresponding to a snap (i.e. sudden
238   catastrophic failure of the adhesive interface) of the entire structure. Both these phenomena are
239   in agreement with empirical observations.

240   The analysis of load-displacement curves revealed that, for all species, the force is
241   mostly given by the elastic deformation of the structure. Reaching a border of the membrane
242   causes a drop in the adhesive force, so that the maximal resistance is often found in the early
243   stages of the delamination process. At low pulling angles, (e.g. 15°) the attachments can sustain
244   high maximal loads due to the stiffness of the dragline. At larger pulling angles (90° and 165°),
245   the mechanical response of the structure is ruled by the interaction between the dragline, the
246   bridge and the plaque. For *H. troglodytes* and *I. villosa*, the plaque is pulled along with the
247   dragline, thus lowering the curve slope by the same amount for both 90° and 165°. For 165° the
248   loading force and the dragline are misaligned, lowering the stress concentrations along the
249   dragline and consequently the elastic energy that can be absorbed. This misalignment is reduced
250   if a detached area appears around the dragline, which allows the *I. villosa* anchorage to have
251   similar maximal pull-off forces for 90° and 180°. This changes for the *T. plumipes*, which has

a soft bridge surrounding the front of the dragline. For a pull-off angle of 90°, the stresses are distributed from the dragline to the bridge and the plaque, which is directly connected at the rear of the dragline: thus, the structural stiffness is given by the dragline-bridge-plaque system. For a pull-off angle of 165°, the stress is concentrated at the front of the attachment and thus the junction between the dragline and the plaque is not involved in delamination. The stressed part is the soft bridge, thus allowing the dragline to align itself to the loading force, distributing stresses along its length and providing high strength. In conclusion, a soft bridge helps the distribution of stresses along the dragline, thus improving the adhesive performance of the structure at high pulling angles, something which is impossible to achieve by varying other parameters. The variations in effective stiffness for increasing extensions overestimate experimental values. This would seem to indicate the presence of geometrical features that allow a more uniform stress redistribution during loading, but are not captured by our model.

To further investigate the dependence of detachment behaviour on geometrical and mechanical characteristics for perpendicular pulling, we varied different parameters in the *T. plumipes* model, like the size and position of the bridge, dragline placement c_d and the ratio between plaque and bridge stiffness E_b/E_p (Tab. 2). We found that for a fixed E_b/E_p the size and position of the bridge had an effect on both the maximal adhesive strength and the slope of the force-extension curve (Fig. 5a). A bridge that was shifted towards the loading point, reflecting the asymmetry of the bridge that is present in *T. plumipes*, could resist the highest force, although the optimal placement depends on many parameters, and is not discussed in detail here. The effect of dragline placement on anchor resistance varied depending on the size and position of the bridge. The empirically observed mechanical behaviour was only obtained in simulations if the bridge surrounded the whole dragline joint and was modelled approximately 100 times softer than the plaque (Fig. 5b). However, this was not the case for more realistic models, where the bridge was positioned asymmetrically with respect to the loading point (Figs. 5c, d). Comparing the latter configurations (*II-IV*) to the one where there is a complete envelopment of the dragline (*I*) we observed that, if a fraction of the dragline is directly connected to the plaque, the stress locations are shifted to the rear plaque (Fig. 5), leading to a better exploitation of the available surface area and higher pull-off forces but a force-displacement slope less dependent from the bridge stiffness. Notice that configuration *III*, where the dragline is also connected to the front plaque, does not lead to a shift in the stress distribution to the rear of the membrane and thus the maximal elongations and pull-off forces are lower than the ones observed in configurations *II* and *IV*.

285   Focusing now on a single configuration, a softer bridge helps this shift of the stress

286 location to the rear of the membrane, but this does not always lead to a higher force: in

287 configurations *II* (Fig. 5c) and *IV* (Fig. 5d), for $c_d = 0.5$ mm and $E_b/E_p = 100$ lower pull-off

288 force are observed because the rear border is reached sooner that the front one. Independent of

289 the configuration, a softer bridge always increased the maximal elongation of the structure.

290

291   **3. Discussion**

292   We found that the mechanical performance of silk anchors varied profoundly between

293 species, and was highest in the derived orb web spiders. These spiders construct large aerial

294 webs, which requires anchorages that resist delamination independent of the pulling angle (10,

295 12, 20). It was previously suggested that the structure of silk anchorages was optimized with

296 the evolution of aerial spider webs, which was primarily attributed to the dragline placement

297 parameter c_d (12). The large sheet webs of the ancient *H. troglodytes* were also partly

298 suspended, but were generally anchored with more lines than orb webs and only occurred in

299 sheltered places such as in caves and in hollow logs, and thus the mechanical requirements to

300 their anchors are probably less stringent. Generally, it can be assumed that the requirements to

301 spin robust anchorages are highest in the orb weaver, were webs are exposed to winds, rain and

302 the impact of large prey items. Such impacts must be shared by few anchor lines, each of which

303 are attached with few anchors. Naturally occurring pulling angles may be more steep and more

304 variable in the suspended webs of *T. plumipes* and *H. troglodytes* than in *K. hibernalis* and *I.*

305 *villosa* that predominantly spin silk lines parallel to the substrate. Both the different selective

306 pressures on anchor robustness and the evolutionary opportunity of anchor enhancement

307 explain the observed inter-species differences in anchor strength and its robustness towards

308 variations in pulling angles.

309   Our results demonstrated that dragline placement is not the only key parameter

310 governing the strength of silk anchors. In addition, both the ratio of anchor and dragline stiffness

311 as well as the nature of the dragline joint as well as bridge position displayed considerable

312 effects. Most noteworthy, the introduction of a significantly softer silk bridge between the

313 dragline and the plaque heavily enhanced the anchor's capacity to resist detachment, regardless

314 of loading angles. Careful consideration in numerical simulations of numerous other

315 mechanical and geometrical parameters indicates that the presence of such a soft bridge is the

316 most likely mechanism that allows to generate the experimentally observed superior behaviour

317 (See S1 for a discussion of parametric tests). An indirect attachment through a soft element is

318 thus excellently suited for flexible objects such as threads.

319   The proposed mechanism of enhanced robustness in anchors with a soft bridge is the

320   differential load sharing between stiff and soft structures, depending on the loading situation.

321   An anchor can sustain higher forces if crack propagation in the adhesive interface is delayed.

322   Once the delamination crack (i.e. the peeling line) reaches one edge of the plaque, the force

323   resistance drops. Thus, not only the size, shape and location of the bridge, but also dragline

324   placement and the ratio between plaque, bridge and dragline stiffness must be well balanced.

325   We assume that of the four species studied here in *T. plumipes* these parameters were better

326   optimized by constant selective pressure on the secure anchorage of large orb webs over the

327   course of hundreds of million years of evolution.

328   Comparable attachment structures, like the byssus threads of mussels, are more rigid

329   and, accordingly, show a high sensitivity towards the pulling angle (21). Mussels bypass this

330   problem by using not only one byssal attachment but a number of byssus threads that are spaced

331   so that the mean pull-off angle is optimized (22). Notably, the byssus threads exhibit a softer

332   domain in the proximal section, which buffers stress peaks under dynamic loading (22).

333   Material gradients also play a role in the performance of the adhesive structures of beetle feet

334   that are used in highly dynamic situations (23). Silk anchors differ from the previous examples

335   by their rapid production and universal application. Our study demonstrates that the

336   combination of stiff and soft elements significantly enhances the robustness of spider web

337   anchorages.

338   It is still not fully understood, why the observed relationship between dragline

339   placement c_d and the anchor strength F_{max}/A was expressed more strongly in the two species

340   that build a bridge into their anchors. While it was possible to adjust our numerical models to

341   approximate the empirical force-distance curves, we could not fully replicate a strong effect of

342   c_d on F_{max} in our simulations with bridge models. Such a relationship was only found if the

343   entire dragline joint was surrounded by the bridge, albeit far less expressed than empirically

344   observed. If an asymmetric bridge geometry was used as in the natural anchors, the effect of c_d

345   on F_{max} was negligible (Fig. 5). Also, the effect was expressed more strongly if the difference

346   in stiffness between bridge and plaque was higher. These results indicate that the geometry,

347   size and mechanical properties of the bridge all affect the capacity of dragline placement to

348   enhance anchor strength. Note that a previous set of simulations considering a simpler geometry

349   that neglected the presence of the bridge in the attachment revealed a larger effect of c_d on F_{max}

350   (12). Simulations on this simplified geometry also showed that a central dragline placement had

351   an effect comparable to that of the bridge on the anchor's sensitivity towards pulling angle, but

352   could not explain the differences in the slopes observed in the comparative pulling tests with *T.*

plumipes. This shows up the difficulties of adopting an appropriate numerical approach, which must balance between (over-)simplification and (over)-complexity (and thus computation ability). For instance, the natural silk membrane likely has constitutive anisotropic and non-linear properties. This may be particularly relevant in the bridge, where anisotropy has a considerable effect on the stress distribution. Furthermore, fracture was neglected in the models, which may lead to an over-estimation of F_{max} in some instances where anchors would naturally fail by fracture. The balance between adhesion and cohesion failure in thin film adhesive micro-composites such as silk anchors is an important problem that should be clarified in future studies.

4. Conclusion

Spiders are masters in the building of web architectures. This can be attributed to the combination of different materials and structures in web anchorage. We have demonstrated that robust attachments are achieved by using a material that is significantly softer than the structural line. The introduction of an additional softer element between the substrate attachment and the line prevents an early failure at steep loading angles, and enhances the versatility of the anchor. This is most pronounced in orb weavers, where the structure and the combination of extensible and stiffer domains are optimized to create a robust system.

From the engineering perspective, spider web anchorages could be a truly inspirational model to design nearly instant, durable and traceless attachment systems that do not require an alteration of the substrate, with a multitude of applications, such as adhesive joints of components in vehicle construction, the flexible fastening of textile roof structures in architecture, safety line anchorages in industrial and recreational climbing, and attaching items to walls in households. Here we have demonstrated the benefit of a two-domain or graded adhesive joint, a principle that it is worth exploring in future applied research.

5. Material and Methods

Material sourcing and fieldwork

Spiders were collected in and around Sydney, New South Wales (*T. plumipes*, *I. villosa*) and Dover, Tasmania (*H. troglodytes*) on public parks or private properties with landlord permission. Samples from *K. hibernalis* were collected from a lab stock at the Technical University of Aachen. Silk anchors were collected on poly-propylene sheets (cut pieces of document protector sheets) that were deposited in the spider's containers and removed after 2-5 days. Single anchors were isolated by cutting the polymer sheet ~1 cm around the sample and carefully cutting or burning (with hot needles) the attached dragline ~2 cm above the membrane. For mounting

387   into the test setup, the polymer sheet with the attached silk anchor was attached to a microscopy glass slide using
388   double-sided tape.

389

390   *Structure and morphometrics of silk anchors*

391   Nine to twenty silk anchors per individual spider were imaged with Leica M205A (Leica Microsystems
392   GmbH, Wetzlar, Germany) and Motic (Motic Inc. Ltd., Hong Kong) stereo microscopes with mounted cameras.

393   Morphometrics of silk anchors was performed on micrographs in *ImageJ* (24). We calculated the dragline
394   placement variable c_d as follows: distance d between the dragline joint (point were the dragline leaves the anchor)
395   and the anterior border of the anchor divided by the longitudinal dimension of the anchor. Details on the
396   morphometric characterization of silk anchors are described in ref. (10).

397

398   *Silk biomechanics*

399   We measured the maximal force (F_{max}) required to pull off a silk anchor from a polypropylene surface as
400   described in detail in ref. (10). Tests were performed under dry lab conditions (~50% relative humidity, 22-26°C).
401   Each silk sample was photographed prior to measurement to determine c_d and A (see above). Primary data was
402   obtained for wild-caught *Hickmania troglodytes* and lab-reared *Kukulcania hibernalis*. Primary data for
403   *Trichonephila plumipes* and *Isopeda villosa* was taken from refs. (10) and (20) and re-analysed. Data of different
404   individuals was pooled for statistical analysis. F_{max}/A was statistically compared between species using pairwise
405   Wilcoxon rank sum tests with FDR alpha correction. To explore the correlation of c_d and F_{max}/A, we fitted sine
406   and linear functions. While the relationship will likely follow a sine function, linear functions provided a similarly
407   good fit (S2), because data for very low and high c_d was sparse or lacking, since they are rarely produced by
408   spiders. We therefore proceeded with linear regression using R 3.5.0. (25).

409

410   *Numerical model*

411   The elastic membrane was modelled by discretising it in a network of elastic bonds (i.e. springs) in a
412   square-diagonal lattice, using a generalized non-linear 3D co-rotational truss formulation(26), as done in Liprandi
413   et al. (14). A homogenization procedure was adopted, imposing the equivalence of the strain energy density of the
414   lattice with that of a corresponding homogeneous membrane (27, 28). The interface was modelled using a Cohesive
415   Zone Model characterized by a 3D traction-separation law $T_i = \Delta_i \frac{\phi}{\delta^2} \cdot \exp\left(-\frac{\Delta_{eff}^2}{\delta^2}\right)$ where ϕ, Δ_{eff} and δ are the
416   work of separation, the crack gap value and the characteristic length (i.e. the gap value corresponding to the
417   maximum traction) (29, 30).

418   A displacement-control procedure was used to simulate the external load. The resulting system of coupled
419   non-linear equations in matrix form was solved using an algorithm based on the Newton-Raphson method (31)
420   implemented in C++. The choice of the crack gap value was made, as already done in literature, to be of the order
421   of the discretization length and consistent with analytical results for axisymmetrical peeling.

422   Two model parameters were calculated using the available empirical data (Tabs. 1, S1). Since the model
423   represents a continuous membrane, we took into account the sparseness of the fibres by recalculating the elastic
424   coefficient $E \cdot t$ by comparing the force-displacement relationship of the numerical model and the empirical results
425   during the purely elastic phase (i.e. before any delamination occurs, and thus without the involvement of adhesive
426   energy). We supposed that during the elastic phase the anchorages would behave as an elastic circular membrane
427   (16) with a Young's modulus between those of the bridge and dragline. Then, we calculated the thickness needed

428   to obtain a force-elongation ratio equal to the empirical one, obtaining values 10 to 100 times lower than the

429   initially estimated ones for all the species. We thus chose to use a thickness equal to 0.1 times the empirical value

430   (see Results section). The work of separation ϕ was then chosen for each silk anchor by comparing the maximal

431   forces and displacements obtained by the numerical simulations with the empirical ones using a trial-and-error

432   scheme for a pull-off angle of $\theta = 90°$ (where the highest proportion of samples failed by total delamination in

433   this loading situation in all three species, allowing us to neglect fracture). We obtained $\phi = 4$ kPa/mm for the *H.*

434   *troglodytes* and the *I. villosa*, and $\phi = 2$ kPa/mm for the *T. plumipes*. The morphology of the anchors was

435   simplified in the models. For the plaque, a rectangular shape was chosen with the dimensions taken as the length

436   and width measured in the samples (see above). In *H. troglodytes* the dragline was model as directly fused with

437   the plaque. In the *I. villosa* model a circular bridge was introduced around the fused dragline, using the same

438   Young's modulus as the plaque (0.22 GPa). In the *T. plumipes* model the bridge centre was positioned closer to

439   the loading point and assigned a Young's modulus of 0.016 GPa, which was 100 times lower than the plaque to

440   simulate the higher extensibility provided by the unstretched bridge fibres (see main text for justification). The

441   exact parameters used are given in Tab. 1 and schematically illustrated in Fig. 6.

442   The pulling procedure is performed as follows: a fixed small displacement is applied at the insertion point

443   at an angle θ. The equilibrium configuration is obtained in quasi-static conditions using an iterative procedure.

444   Another fixed small displacement is then applied in the same point at the same angle, and so forth. The simulation

445   stops when one of the following becomes true: (a) total delamination is reached; (b) a mechanical instability

446   resulting in a snapping of a part of the membrane is reached.

447   To observe how the geometrical and mechanical properties change the mechanical response of the elastic

448   membrane, two explorative parametrical study were conducted. We studied the effect of the dragline width, the

449   dragline length, the adhesive energy per area, the anchorage thickness and the stress-strain relationship of the silk

450   for a disc with of an area of 1.4 mm x 1.6 mm plaque, with a dragline of length equal to 0.4 mm inserted at 0.5

451   mm from the front border. The results are shown in S1. For the *T. plumipes* model, we studied the geometrical and

452   mechanical parameters of the bridge by varying the dragline attachment and bridge shapes as follows: three

453   different centres of the bridge were used: at the insertion point c_d, at half the dragline length $(c_d + \frac{l_d}{2})$, and close

454   to the half of the dragline length $(c_d + \frac{l_d}{2} - \Delta b)$; and four different bridge radii (Tab. 2). The bridge Young's

455   modulus E_b was set to be $E_b = 0.1\,E_p$ or $E_b = 0.01\,E_p$, where E_p is the Young's modulus of the plaque. Three

456   different values of c_d ($[0, 0.25, 0.5]$ mm) were used for each bridge configuration.

457

458

was funded by the Deutsche Forschungsgemeinschaft (JO1464/2-1). NMP was supported by the Italian Ministry of Education, University and Research (MIUR) under the "Departments of Excellence" grant L.232/2016, the ARS01-01384-PROSCAN Grant and the PRIN-20177TTP3S Grant.

Author contributions

JOW, FB and NMP devised, led and administered the project. JOW and ACJ performed the empirical study. DL developed the numerical model and carried out the numerical simulations. JOW, DL and FB wrote the manuscript and NMP reviewed it. All authors critically revised the manuscript and approved its final version.

Competing Interests

The authors declare that they have no conflict of interests.

Data accessibility

Data are reported in the supplemental information (S1, S2) and the main text of this paper.

References

1. Eder M, Amini S, & Fratzl P (2018) Biological composites—complex structures for functional diversity. *Sci China Life Sci* 362(6414):543-547.
2. Wolff JO, Grawe I, Wirth M, Karstedt A, & Gorb SN (2015) Spider's super-glue: thread anchors are composite adhesives with synergistic hierarchical organization. *Soft Matter* 11(12):2394-2403.
3. Hagenau A, Suhre MH, & Scheibel TR (2014) Nature as a blueprint for polymer material concepts: Protein fiber-reinforced composites as holdfasts of mussels. *Progress in polymer science* 39(8):1564-1583.
4. Rizzo N*, et al.* (2006) Characterization of the structure and composition of gecko adhesive setae. 3(8):441-451.
5. Heepe L, Xue L, & Gorb SN (2017) Bio-inspired structured adhesives. *Biologically-Inspired Systems* 9:1-347.
6. Wolff JO, Wells D, Reid CR, & Blamires SJ (2017) Clarity of objectives and working principles enhances the success of biomimetic programs. *Bioinspir Biomim* 12(5):051001.
7. Sahni V, Harris J, Blackledge TA, & Dhinojwala A (2012) Cobweb-weaving spiders produce different attachment discs for locomotion and prey capture. *Nat Commun* 3(1):1-7.
8. Wolff JO, Řezáč M, Krejčí T, & Gorb SN (2017) Hunting with sticky tape: functional shift in silk glands of araneophagous ground spiders (Gnaphosidae). *J Exp Biol* 220:2250-2259.
9. Greco G, Wolff JO, & Pugno NM (2020) Strong and tough silk for resilient attachment discs: the mechanical properties of piriform silk in the spider Cupiennius salei (Keyserling, 1877). *Frontiers in Materials* 7:138.
10. Wolff JO & Herberstein ME (2017) 3D-printing spiders: back-and-forth glue application yields silk anchorages with high pull-off resistance under varying loading situations. *J R Soc Interface* 14:20160783.
11. Kendall K (1975) Thin-film peeling - The elastic term. *Journal of Physics D: Applied Physics* 8(13):1449-1452.
12. Wolff JO*, et al.* (2019) Evolution of aerial spider webs coincided with repeated structural optimization of silk anchorages. *Evolution* 73(10):2122-2134.
13. Grawe I, Wolff JO, & Gorb SN (2014) Composition and substrate-dependent strength of the silken attachment discs in spiders. *J. R. Soc. Interface* 11(98):1742-5662.
14. Liprandi D, Bosia F, & Pugno NM (2020) A theoretical-numerical model for the peeling of elastic membranes. *J Mech Phys Solids* 136:103733.
15. Pugno NM (2011) The theory of multiple peeling. *Int J Fracture* 171(2):185-193.
16. Afferrante L, Carbone G, Demelio G, & Pugno N (2013) Adhesion of Elastic Thin Films: Double Peeling of Tapes Versus Axisymmetric Peeling of Membranes. *Tribol Lett* 52(3):439-447.
17. Swanson B, Blackledge T, Beltrán J, & Hayashi C (2006) Variation in the material properties of spider dragline silk across species. *Applied Physics A* 82(2):213-218.
18. Piorkowski D*, et al.* (2018) Ontogenetic shift toward stronger, tougher silk of a web-building, cave-dwelling spider. *J Zool* 304(2):81-89.

521   19.   Craig HC, Piorkowski D, Nakagawa S, Kasumovic MM, & Blamires SJ (2020) Meta-analysis reveals
522   materiomic relationships in major ampullate silk across the spider phylogeny. *J R Soc Interface*
523   17(170):20200471.
524   20.   Wolff JO, van der Meijden A, & Herberstein ME (2017) Distinct spinning patterns gain differentiated
525   loading tolerance of silk thread anchorages in spiders with different ecology. *Proceedings of the Royal*
526   *Society B: Biological Sciences* 284:20171124.
527   21.   Desmond KW, Zacchia NA, Waite JH, & Valentine MT (2015) Dynamics of mussel plaque detachment.
528   *Soft Matter* 11(34):6832-6839.
529   22.   Qin Z & Buehler MJ (2013) Impact tolerance in mussel thread networks by heterogeneous material
530   distribution. *Nat Commun* 4:2187.
531   23.   Peisker H, Michels J, & Gorb SN (2013) Evidence for a material gradient in the adhesive tarsal setae of
532   the ladybird beetle Coccinella septempunctata. *Nat Commun* 4(1):1-7.
533   24.   Schneider CA, Rasband WS, & Eliceiri KW (2012) NIH Image to ImageJ: 25 years of image analysis.
534   *Nat methods* 9(7):671-675.
535   25.   Team RC (2016) R: A language and environment for statistical computing. . (R Foundation for Statistical
536   Computing, Vienna, Austria).
537   26.   Cook RD, Malkus DS, & Plesha ME (2001) *Concepts and applications of finite element analysis* (John
538   Wiley & Sons) p 630.
539   27.   Ostoja-Starzewski M (2002) Lattice models in micromechanics. *Applied Mechanics Reviews* 55(1):35-
540   60.
541   28.   Brely L, Bosia F, & Pugno NM (2015) A hierarchical lattice spring model to simulate the mechanics of
542   2-D materials-based composites. *Frontiers in Materials* 2:51.
543   29.   Sauer RA (2016) A survey of computational models for adhesion. *The Journal of Adhesion* 92(2):81-120.
544   30.   Xu X-P & Needleman A (1993) Void nucleation by inclusion debonding in a crystal matrix. *Modelling*
545   *and Simulation in Materials Science and Engineering* 1(2):111.
546   31.   Ostrowski AM (1973) The Newton-Raphson Method," Pure Appl. Math. *Third Edition of Solution of*
547   *Equations and Systems of Equations,* Pure and Applied Mathematics, ed Ostrowski AM (Elsevier), Vol
548   9, pp 53-55.
549
550

551 **Tables**

552

553 **Tab. 1. Geometrical properties of models used in numerical simulations.** For a schematic
554 illustration of the geometrical parameters see Fig. 6a. Abbreviations: b, centre of circular bridge
555 (x, y); d, location of dragline insertion point (distance from front edge); E_b, Young's modulus
556 of the plaque; E_p, Young's modulus of the plaque; E_d, Young's modulus of the dragline; l_p,
557 plaque (membrane) length; l_{dl}, length of attached dragline; r_b, radius of the circular bridge;
558 t_{num}, membrane thickness; t_{num}/t_{emp}, relative density (fibre density); w_p, maximal width of
559 plaque (membrane).

560

	l_p (mm)	w_p (mm)	l_{dl} (mm)	d (mm)	E_p (GPa)	E_d (GPa)	E_b (GPa)	b (mm)	r_b (mm)	t_{num} (µm)	t_{num}/t_{emp}
H. troglodytes	2.4	2.6	1.2	0.5	0.25	10	-	-	-	1	0.1
I. villosa	2.1	1.6	1.3	0.4	0.22	10	0.22	(1.0, 0.8)	0.7	1	0.1
T. plumipes	1.4	1.5	0.4	0.5	1.68	15	0.0168	(0.62, 0.75)	0.25	1.5	0.1

561

562 **Tab. 2. Properties of models used in the parametrical study on the effect of bridge
563 geometry and softness on pull-off forces.** For a schematic illustration of the geometrical
564 parameters see Fig. 6a. Abbreviations: b, centre of circular bridge; E_p, Young's modulus of the
565 plaque; E_d, Young's modulus of the dragline; l_p, plaque (membrane) length; l_{dl}, length of
566 attached dragline; r_b, radius of the circular bridge; t_{num}, membrane thickness; w_p, maximal
567 width of plaque (membrane). d varied for every set of simulations (I-IV) between the following
568 values: 0 mm, 0.25 mm, 0.5 mm. E_b varied for every set of simulations (I-IV) between the
569 following values: 0.168 GPa, 0.0168 GPa.

570

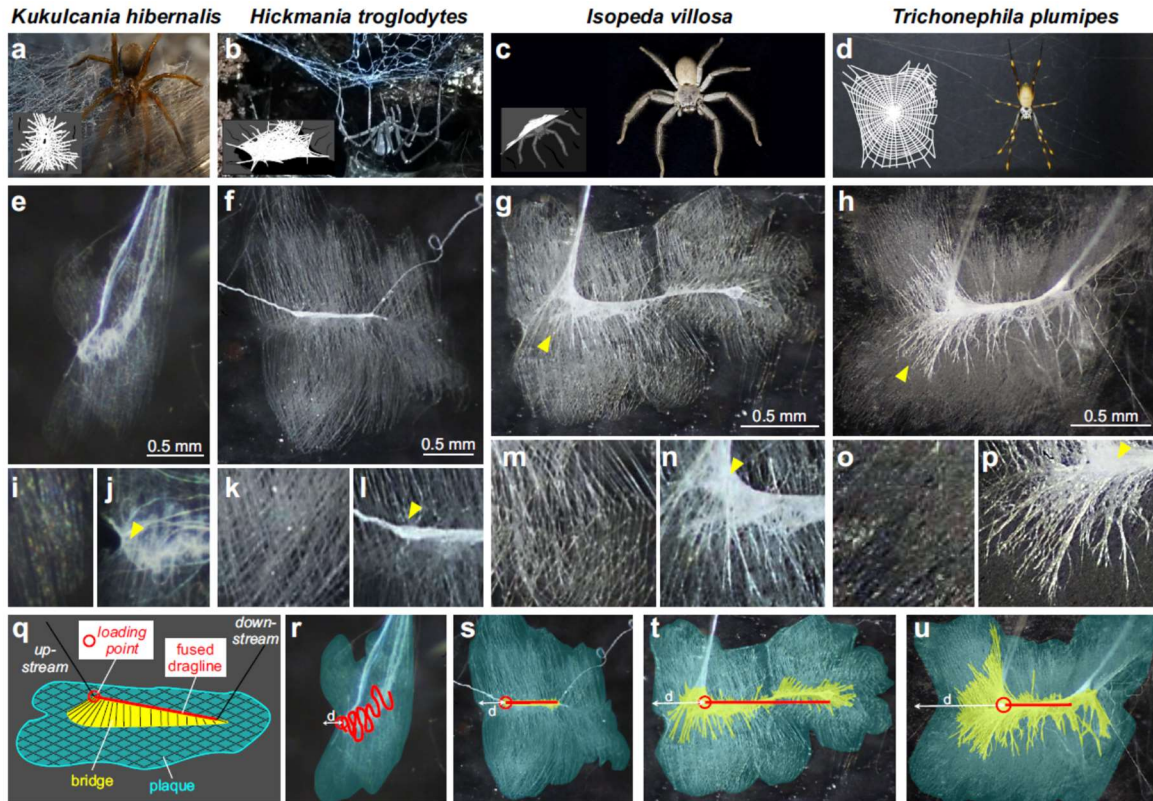|	l_p (mm)	w_p (mm)	l_{dl} (mm)	E_p (GPa)	E_d (GPa)	t_{num} (µm)	b (mm)	r_b (mm)
I							$d + 0.2$	0.25
II	1.4	1.5	0.4	1.68	15	1.5	d	0.2
III							$d + 0.12$	0.125
IV							$d + 0.12$	0.25

571

Fig. 1. Morphology of spider silk line anchors.   (a, e, i, j, r) Southern house spider (*Kukulkania hibernalis*, Filistatidae). (b, f, k, l, s) Tasmanian cave spider (*Hickmania troglodytes*, Austrochilidae). (c, g, m, n, t) Huntsman (*Isopeda villosa,* Sparassidae). (d, h, o, p, u) Golden orb weaver (*Trichonephila plumipes*, Araneidae). (a-d) Photos of spider species used in the tests, and for which anchors are displayed in columns below. Schematic insets display web or shelter architecture. Note that a-c are substrate bound silk structures with anchor lines meeting the substrate at low angles, whereas d is an aerial (suspended) web with anchor lines meeting the substrate at a steep angle. (e-h) Total view of silk anchor on a transparent substrate, viewed from above in a stereo microscope with reflective light. Yellow arrowhead points to the 'bridge' element. (i, k, m, o) Detail of plaque. Note the lattice-like arrangement of piriform silk fibres and the higher fibre density in *T. plumipes*. (j, l, n, p) Detail of dragline joint. Yellow arrowhead points to the loading point. Note the piriform fibre network (bridge) in n and p. (q) Schematic illustration of silk anchor as viewed at an angle. (r-u) same as in e-h but with the different elements marked (same colour code as in q): red, fused dragline (schematically); blue, plaque; yellow, bridge; red circle, loading point (point where the dragline leaves the anchor); d, distance between the loading point and the plaque edge (dragline placement $c_d = d/l_p$, where l_p is the plaque length).
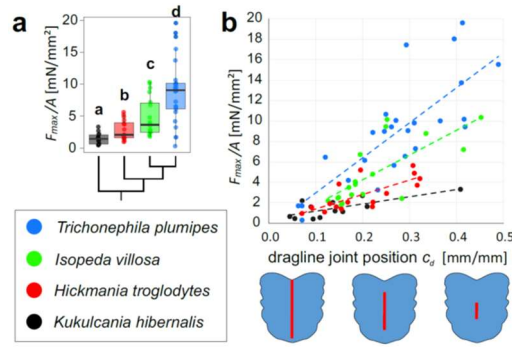
597

Fig. 2. Comparison of web anchor performance. (a) Measured anchor strength F_{max}/A for perpendicular pulling ($\theta = 90°$) in four species of spiders. Below, a simplified cladogram of the species relationships. Different letters above the plots indicate different groups with a significance level of 0.05. (b) F_{max}/A against dragline placement c_d for each of the species (same colour code as in a). Schematic drawings below the diagram illustrate silk anchors with different c_d values (as viewed from above) according to the diagram's x-axis (fused dragline in red, piriform silk in blue).

609
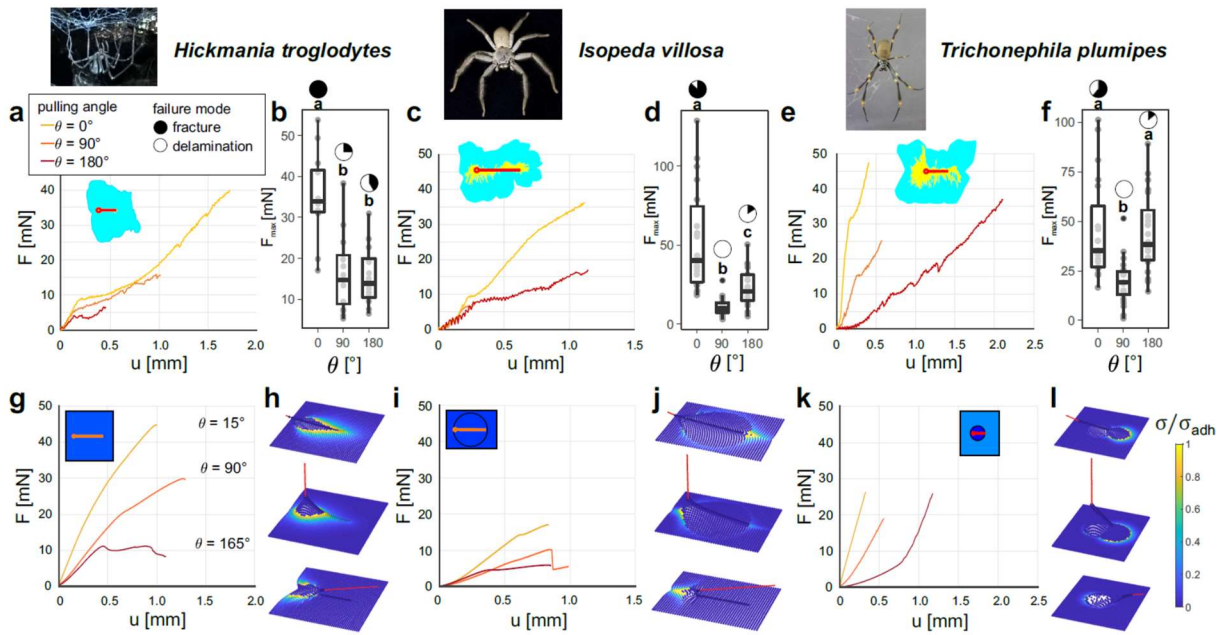
Fig. 3. Pull-off dynamics of silk anchors in three spider species. (a-f) Results of empirical pull-off tests. (g-l) Results of numerical simulations. (a-b, g-h) Tasmanian cave spider (*H. troglodytes*). (c-d, i-j) Huntsman (*I. villosa*). (e-f, k-l) Golden orb weaver (*T. plumipes*). (a, c, e) Exemplary force-extension curves for three different pulling angles (θ). Note that the initial slope that indicates the stiffness of the structure, is similar between loading situations in *H. troglodytes* and *I. villosa*, but decreases with increasing pulling angles in *T. plumipes*. Inset schematics illustrates anchor morphology as viewed from above (see Fig. 1 for details), not to scale. Different letters above the plots indicate different groups with a significance level of 0.05. (b, e, h) Maximal pull-off forces (F_{max}) depending on dragline pulling angle. Boxplots indicate the median (thick middle line), the interquartile range (the boxes), extreme values (whiskers) and out-of-range outliers (dark dots), with all original data points in dark grey (jitter plots). Pie charts above boxes illustrate the proportion of samples that failed by rupture (black) versus

622 complete surface detachment (white). (g, i, k) Simulated force-extension curves with numerical
623 models using the parameters measured in the natural anchors. Colour code of the curves for
624 different pulling angles as in a, c, e. Inset schematics illustrates view of model from above (see
625 Fig. 4 for details), not to scale. (h, j, l) Three dimensional rendering of models at an intermediate
626 displacement ($u/u_{max} \cong 0.8$) at $\theta = 15°$, $\theta = 90°$ and $\theta = 165°$ (from top to bottom). The colours
627 indicate the relative adhesive stress field (σ/σ_{adh}), with blue indicating low stress and yellow
628 maximal stress (σ_{adh}) causing delamination (see legend right of l). The red line illustrates the
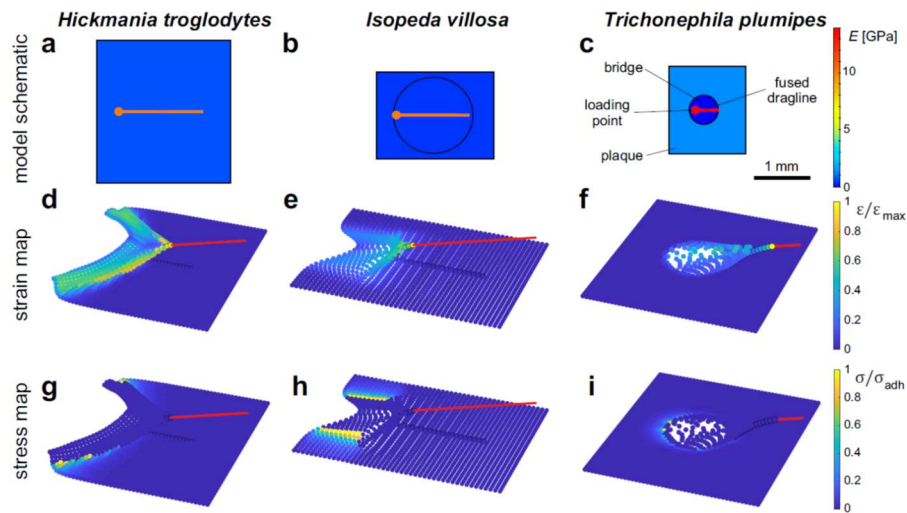629 pulled upstream dragline.

630
631
632

633

634 **Fig. 4. Simulated behaviour of silk anchor under a steep loading angle.** Species models
635 grouped per column. (a-c) Schematic illustration of model, as viewed from above, all same
636 scale. Colours indicate the stiffness (E) of each element (see legend to the right). (d-i) Three-
637 dimensional renderings of models at F_{max} loaded at $\theta = 165°$. (d-f) Colours indicate the relative
638 strain field ($\varepsilon/\varepsilon_{max}$), with ε indicating the mean strain of the springs representing a section of
639 the membrane, ε_{max} indicating the maximal strain at the correspondent timestep, blue colours
640 indicating low strain and yellow indicating high strain (see legend to the right). (g-i) Colours
641 indicate the adhesive stress field (σ/σ_{adh}), with σ indicating the stress in the springs at the
642 adhesive interface, σ_{adh} indicating the stress at which delamination occurs, blue colours
643 indicating low stress and yellow indicating high stress (see legend to the right). The anchors of
644 *H. troglodytes* and *I. villosa* fail by delamination (peeling), whereas the anchor of *N. plumipes*
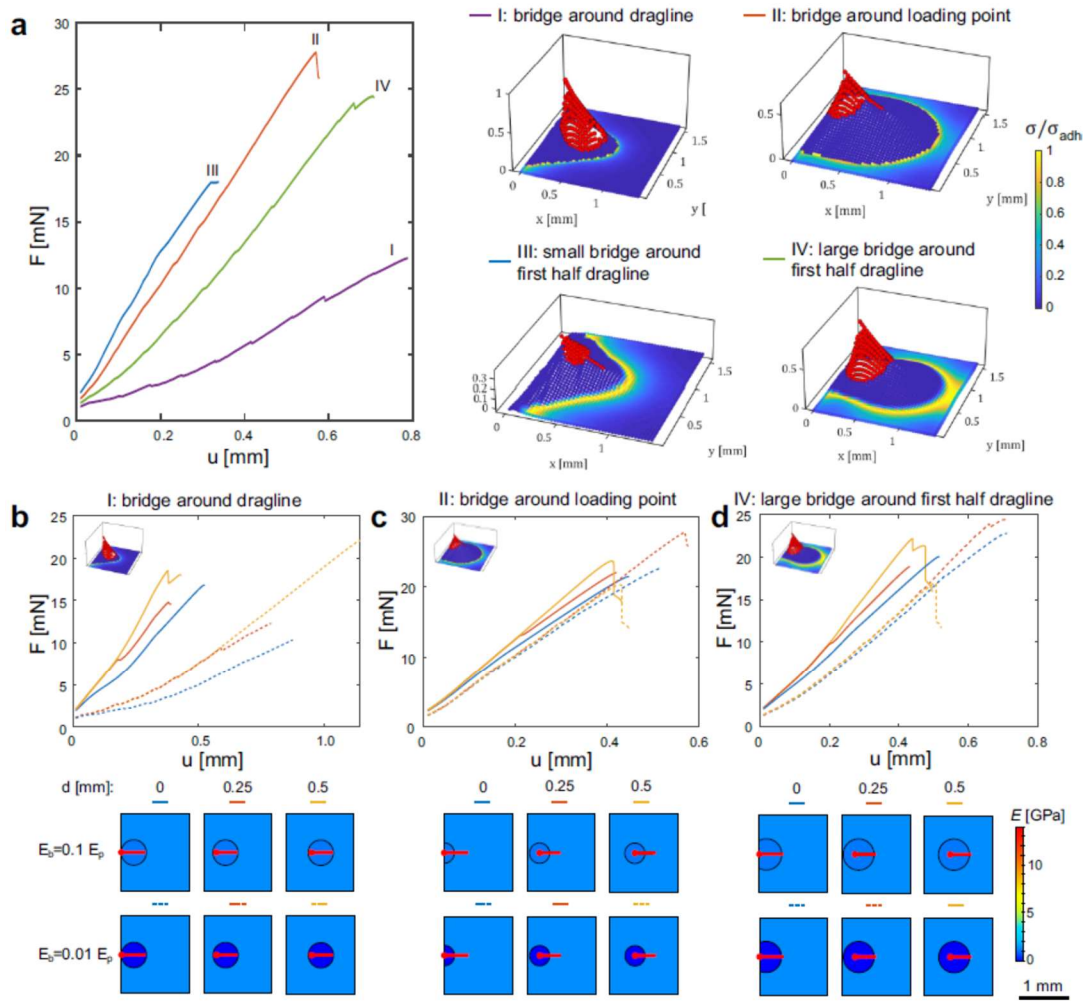645 detaches by a sudden catastrophic failure ('snap') of the adhesive interface.

646
647
648

649

Fig. 5. Effect of bridge structure and stiffness, and dragline placement on anchor resistance. (a) Simulated force-extension for a $\theta = 90°$ using different bridge geometries. Three-dimensional renderings on the right illustrate the different models under load, with red illustrating the bridge and dragline joint, and blue and yellow shading indicating interfacial stress in the plaque (peeling line). (b-d) Simulated force extension curves for varying dragline placement c_d and bridge softness. Solid lines represent the force-extension curves of models with $E_b = 0.1\ E_p$ and dashed lines of models with $E_b = 0.01\ E_p$ (i.e. softer bridge). The morphology and mechanical properties of the corresponding models are schematically illustrated below, as viewed from above (same conventions as in Fig. 4).
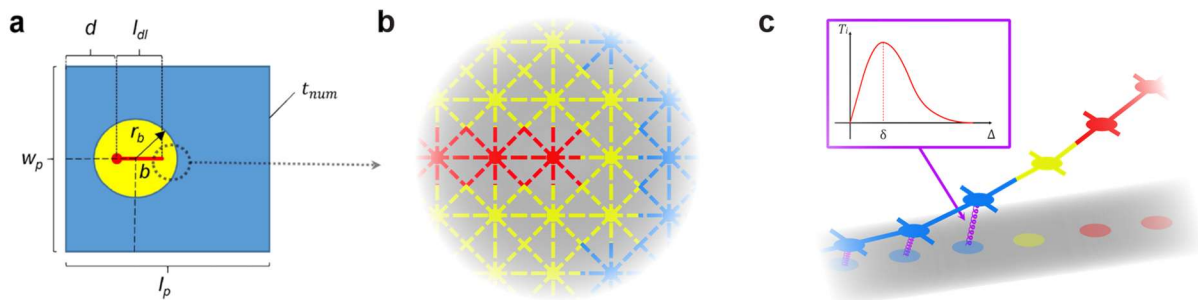
659

660

661

662

Fig. 6. Schematic illustration of properties simulated in the numerical models. The attached plaque is coloured blue, the bridge (initially detached, softer part of plaque) in yellow, and the fused part of the dragline in red. Different elastic and adhesive properties were assigned to each of these three parts. (a) Geometrical parameters of anchor models. (b) Schematic representation of the Lattice Spring Model (LSM). Elastic springs connect the nodes. Springs connecting two different areas have a stiffness equal to the mean of the two assigned values. (c) Schematic representation of the cohesive model. Each plaque node is connected to its initial position on the substrate by a traction-separation law.

Supplemental information

S1. Results of parametric studies and information on the inference of mechanical properties of silk anchor parts for in silico experiments (pdf).

S2. F_{max} and F_a data for four species of spiders (csv).